

Geophysical Journal International (May, 2013) **193** (2): 678-693. doi: 10.1093/gji/ggt027
The journal version is available at: <http://gji.oxfordjournals.org/content/193/2/678>

A parallel finite-element method for 3D controlled-source electromagnetic forward modeling

Vladimir Puzyrev, Jelena Koldan, Josep de la Puente, Guillaume Houzeaux, Mariano Vázquez and José María Cela.

Department of Computer Applications in Science and Engineering, Barcelona Supercomputing Center.

ABSTRACT

We present a nodal finite-element method that can be used to compute in parallel highly accurate solutions for 3-D controlled-source electromagnetic forward modeling problems in anisotropic media. Secondary coupled-potential formulation of Maxwell's equations allows to avoid the singularities introduced by the sources, while completely unstructured tetrahedral meshes and mesh refinement support an accurate representation of geological and bathymetric complexity and improve the solution accuracy. Different complex iterative solvers and an efficient preconditioner based on the sparse approximate inverse are used for solving the resulting large sparse linear system of equations. Results are compared with the ones of other researchers in order to check the accuracy of the method. We demonstrate the performance of the code in large problems with tens and even hundreds of millions of degrees of freedom. Scalability tests on massively parallel computers show that our code is highly scalable.

Keywords: Numerical solutions; Numerical approximations and analysis; Electromagnetic theory; Marine electromagnetics.

1 INTRODUCTION

The marine controlled-source electromagnetic (CSEM) method is nowadays a well-known geophysical exploration tool in the offshore environment and a commonplace in the industry (e.g., Constable & Srnka 2007; Constable 2010; Weitemeyer et al. 2010). In CSEM, also referred to as seabed logging (SBL) (Eidesmo et al. 2002), the sub-seafloor structure is explored by emitting low-frequency signals from a high-powered electric dipole source close to the seafloor. By studying the

received signal, thin resistive layers beneath the seafloor could be detected at scales of a few tens of meters to depths of several kilometers (Andreis & MacGregor 2008).

During the last decade, CSEM has been considered as an important tool for reducing ambiguities in data interpretation and reducing exploratory risk. The academic and industrial development of the method is discussed in the review paper by Edwards (2005) and the recent paper by Key (2012). The most popular numerical modeling techniques applied to forward modeling of electromagnetic problems are finite-difference (FD) and finite-element (FE) methods, although other methods have been marginally applied too, such as integral-equation methods (e.g., Wannamaker et al. 1984; Avdeev et al. 1997; Zhdanov & Fang 1997) and the finite-volume method (Haber et al. 2000; Weiss & Constable 2006). A more detailed description can be found, for example, in Avdeev (2005) and Borner (2010). Advances in electromagnetic induction techniques for near-surface investigations made since 2007 are discussed in the recent review paper by Everett (2012).

FD techniques have been widely used in solving 2D and 3D time-domain and frequency-domain problems (e.g., Newman & Alumbaugh 1995; Davydycheva et al. 2003; Abubakar et al. 2008; Commer & Newman 2008; Sasaki & Meju 2009; Streich et al. 2011). The traditional FD method is easier to implement and maintain than the FE method, but it is based on structured rectangular grids. This means that local grid refinement is not possible and any grid size adaptation has a large effect on the overall computational resources needed. Furthermore, complex structures cannot be accurately honored with rectangular elements, which is known to have a serious impact on the quality of the solutions, for example in the case of seafloor variations that also can greatly affect EM responses (Schwablenberg & Edwards 2004). For problems displaying a certain geometrical complexity, the FE method is generally preferred because it has an advantage of naturally supporting unstructured meshes. These meshes allow for an accurate representation of seafloor bathymetry or large conductivity contrasts without requiring small grid elements in the entire grid but only in the places where better resolution is required.

The FE method has long been used by the applied mathematics and solid mechanics communities and during the last two decades has been applied to EM geophysical problems (Unsworth et al. 1993; Badea et al. 2001; MacGregor et al. 2001; Mitsuhata & Uchida 2004; Key & Weiss 2006; Li & Key 2007; Franke et al. 2007; Li & Dai 2011; Farquharson & Mienopust 2011). A major obstacle for a broader adoption of the FE method was that the standard nodal method does not correctly represent the discontinuity of normal electric field component at material interfaces. Some recent approaches to CSEM (Mukherjee & Everett 2011; Schwarzbach et al. 2011; da Silva et al. 2012; Um et al. 2012) are based on specialized vector or edge finite elements (Nédélec 1986), which overcome this obstacle and correctly represent field discontinuities at the interfaces. Alternatively, various formulations in electromagnetic potentials (Biro & Preis 1989) have been used in nodal FE

methods, also resulting in a good convergence behavior for near-static problems (Haber et al. 2000). Other advantages and disadvantages of the FE method, structured and unstructured meshes in electromagnetic geophysical problems, as well as recent developments in the field are described by Key & Ovall (2011).

In this paper we consider a nodal potential-based FE method for 3D CSEM forward modeling. The paper is organized as follows. In Section 2, we introduce the problem formulation which follows and expands the approach of Badea et al. (2001) for marine CSEM and anisotropic media. Implementation details, including the generation of the mesh and primary potentials, effective preconditioner for solving the system, parallelization and post-processing are presented in Section 3. In Section 4, we show three numerical examples which illustrate the agreement between our method, analytic solutions and the results of other researchers, and a complex synthetic model with bathymetry, followed by a convergence study and scalability tests. Finally, in Section 5, we discuss the method's potentials and outline some future applications.

2 PROBLEM FORMULATION

FE solutions to electromagnetic problems can be formulated in terms of electric and magnetic fields (\mathbf{E}, \mathbf{H}) or through coupled vector-scalar potentials ($\mathbf{A}-\Phi$ or $\mathbf{T}-\Omega$). Advantages and disadvantages of both formulations are described in Badea et al. (2001). Briefly, the most common difficulties of 3D EM modeling with nodal FE method are: domain discretization that supports discontinuous normal component and continuous tangential component of the electric field at material interfaces, spurious modes that may appear in the solution, accurate representation of the source and modeling the air region in shallow-water marine CSEM simulations.

In this paper, the physical problem is formulated in terms of secondary Coulomb-gauged EM potentials (Badea et al. 2001). Assuming harmonic time dependence $e^{-i\omega t}$, the diffusive Maxwell's equations for the electromagnetic field (at low frequencies when displacement currents can be neglected since $\sigma \gg \omega\epsilon$) are:

$$\nabla \times \mathbf{E} = i\omega\mu_0 \mathbf{H}, \quad (1)$$

$$\nabla \times \mathbf{H} = \mathbf{J}_s + \bar{\sigma}\mathbf{E}, \quad (2)$$

where ω is the angular frequency, the magnetic permeability is assumed to be equal to the free space value μ_0 since variations in it are rare (Commer & Newman 2008), \mathbf{J}_s is the source current distribution, while the ohmic conduction term $\bar{\sigma}\mathbf{E}$ describes the induced currents inside the Earth.

The induction and magnetic field vectors are related by the constitutive equation $\mathbf{B} = \mu_0 \mathbf{H}$. $\bar{\sigma}(\mathbf{r})$ is the electric conductivity tensor varying in three dimensions. As noted by Constable (2010), “the marine CSEM community variously ignores electrical anisotropy or declares it to be all-important”. Since in marine environments the formation is typically anisotropic and ignoring this fact affects heavily CSEM data and inversion results, we consider an anisotropic conductivity model. Transverse anisotropy corresponds to many situations encountered in actual geologic basins (Newman et al. 2010):

$$\bar{\sigma} = \begin{pmatrix} \sigma_x & 0 & 0 \\ 0 & \sigma_y & 0 \\ 0 & 0 & \sigma_z \end{pmatrix}, \quad (3)$$

where $\sigma_x = \sigma_y = \sigma_h$ is the horizontal conductivity and $\sigma_z = \sigma_v$ denote the vertical conductivity. The present approach also can be used in the case of generalized anisotropy when the tensor has six independent elements. Since it is symmetric (Weiss & Newman 2002; Løseth & Ursin 2007), the resulting FE matrix also will retain its symmetry.

The electromagnetic fields \mathbf{E} and \mathbf{H} are expressed in terms of a magnetic vector potential \mathbf{A} and an electric scalar potential Ψ as:

$$\mathbf{B} = \nabla \times \mathbf{A}, \quad (4)$$

$$\mathbf{E} = i\omega(\mathbf{A} + \nabla\Psi). \quad (5)$$

To guarantee the uniqueness of the vector potential \mathbf{A} , we apply the Coulomb gauge condition $\nabla \cdot \mathbf{A} = 0$ in combination with proper boundary conditions (Biro & Preis 1989). Substituting expressions (4) and (5) into (2), we obtain a curl-curl equation, but with incorporation of the Coulomb gauge, the vector Laplacian operator replaces the curl-curl operator and we get the vector Helmholtz equation:

$$\nabla^2 \mathbf{A} + i\omega\mu_0\bar{\sigma}(\mathbf{A} + \nabla\Psi) = -\mu_0 \mathbf{J}_s, \quad (6)$$

which has a very stable discretized form. The auxiliary equation:

$$\nabla \cdot [i\omega\mu_0\bar{\sigma}(\mathbf{A} + \nabla\Psi)] = 0, \quad (7a)$$

must be solved simultaneously with (6) in order to keep all physical conditions satisfied. In Badea et al. (2001), equation (7a) was obtained under the assumption that $\nabla \cdot \mathbf{J}_s = 0$, which does not hold for sources such as an electric dipole. The more general form of this equation is

$$\nabla \cdot [i\omega\mu_0\bar{\sigma}(\mathbf{A} + \nabla\Psi)] = -\nabla \cdot [\mu_0\mathbf{J}_s]. \quad (7b)$$

A secondary potential formulation is used in order to avoid singularities that might be introduced by sources. Instead of having it explicitly in (6) and (7b), a source of arbitrary shape, complexity, and orientation can be introduced by defining a set of known primary potentials (\mathbf{A}_p, Ψ_p) . Normally, primary (or background) potentials are analytic expressions for induction in a homogeneous formation of constant electrical conductivity σ_p or in horizontally layered models.

The secondary (or scattered) EM potentials are defined by:

$$\mathbf{A} \equiv \mathbf{A}_p + \mathbf{A}_s, \quad \Psi \equiv \Psi_p + \Psi_s. \quad (8)$$

Finally, the governing equations become:

$$\nabla^2\mathbf{A}_s + i\omega\mu_0\bar{\sigma}(\mathbf{A}_s + \nabla\Psi_s) = -i\omega\mu_0\Delta\bar{\sigma}(\mathbf{A}_p + \nabla\Psi_p), \quad (9)$$

$$\nabla \cdot [i\omega\mu_0\bar{\sigma}(\mathbf{A}_s + \nabla\Psi_s)] = -\nabla \cdot [i\omega\mu_0\Delta\bar{\sigma}(\mathbf{A}_p + \nabla\Psi_p)], \quad (10)$$

where: $\Delta\bar{\sigma} \equiv \bar{\sigma} - \bar{\sigma}_p$ and $\bar{\sigma}_p(\mathbf{r})$ is the background conductivity tensor, which is already known. In the original formulation, based on (7a), the conductivity term in the right-hand side of (10) was $\bar{\sigma}$ instead of $\Delta\bar{\sigma}$.

As stated above, the uniqueness of the vector potential \mathbf{A} is guaranteed by using the Coulomb gauge and appropriate boundary conditions (Biro & Preis 1989). We assume that boundaries of the domain are located far away from the transmitter, at the distance where EM fields have a negligible value, and impose homogeneous Dirichlet boundary conditions on the outer boundary Γ :

$$(\mathbf{A}_s, \Psi_s) \equiv (\mathbf{0}, 0) \text{ on } \Gamma. \quad (11)$$

The equations (9-10) together with the boundary conditions (11) constitute the coupled potential formulation of Maxwell's equations for dipole or loop sources in anisotropic media.

2.1 Finite-element analysis

In order to obtain a numerical solution of a partial differential equation, it is necessary to discretise the equation, which is, by nature, continuous, using some discretisation technique – in our case, we use the FE method (Burnett 1987). Since we formulate the physical problem in terms of

potentials, we use nodal finite elements. In the case of a problem formulated using field vectors, edge elements should be chosen (Monk 2003).

The weak solution (see Badea et al. (2001) for details) is the set of scalar functions $(A_{sx}, A_{sy}, A_{sz}, \Psi_s)$ which satisfies the volume-integrated equations:

$$\begin{aligned} -(\nabla \eta, \nabla A_{sx})_\Omega + i\omega\mu_0 \left(\sigma_x \eta, A_{sx} + \frac{\partial \Psi_s}{\partial x} \right)_\Omega &= -i\omega\mu_0 (\Delta \sigma_x \eta, A_{px})_\Omega, \\ -(\nabla \eta, \nabla A_{sy})_\Omega + i\omega\mu_0 \left(\sigma_y \eta, A_{sy} + \frac{\partial \Psi_s}{\partial y} \right)_\Omega &= -i\omega\mu_0 (\Delta \sigma_y \eta, A_{py})_\Omega, \\ -(\nabla \eta, \nabla A_{sz})_\Omega + i\omega\mu_0 \left(\sigma_z \eta, A_{sz} + \frac{\partial \Psi_s}{\partial z} \right)_\Omega &= -i\omega\mu_0 (\Delta \sigma_z \eta, A_{pz})_\Omega, \\ -i\omega\mu_0 (\bar{\sigma} \nabla \eta, \mathbf{A}_s)_\Omega - i\omega\mu_0 (\bar{\sigma} \nabla \eta, \nabla \Psi_s)_\Omega &= i\omega\mu_0 (\Delta \bar{\sigma} \nabla \eta, \mathbf{A}_p)_\Omega. \end{aligned} \quad (12)$$

In (12) we have omitted the terms with primary scalar potential since for dipole and loop sources $\Psi_p \equiv 0$. Test function $\eta(\mathbf{r})$ is continuous, vanishes on the boundary, and has square-integrable spatial derivatives. The shorthand notation is used for volume integrals

$$(u, v)_\Omega \equiv \int_\Omega u v d\Omega, \quad (\nabla u, \nabla v)_\Omega \equiv \int_\Omega \nabla u \cdot \nabla v d\Omega. \quad (13)$$

In the derivation of the last equation of (12) we used the identity

$$\int_\Omega u (\nabla \cdot \mathbf{A}_s) d\Omega \equiv - \int_\Omega \nabla u \cdot \mathbf{A}_s d\Omega + \text{surface terms}. \quad (14)$$

Surface integrals in the weak formulation vanish due to the homogeneous boundary conditions. The electric conductivity varies throughout the domain, however we assume that it is constant inside of each element. The discretisation of the differential equation produces the system of linear algebraic equations:

$$\mathbf{K} \mathbf{u} = \mathbf{b}. \quad (15)$$

This resultant system approximates the partial differential equation, hence its solution is an approximate, i.e. numerical, solution of the original continuous problem. Considering that we use nodal finite elements, the unknowns are connected to the vertexes of the elements. As already described, there are four scalar functions to be determined, which means that there are 4 degrees of freedom in each node. If the mesh has N interior nodes, there are $4N$ unknowns to be determined.

\mathbf{K} is a $4N \times 4N$ sparse complex matrix consisting of 4×4 blocks given by

$$\mathbf{K}_{ij} = \begin{pmatrix} \left(-(\nabla \alpha_i, \nabla \alpha_j)_\Omega + i\omega\mu_0(\bar{\sigma}\alpha_i, \alpha_j)_\Omega \right) I_{33} & i\omega\mu_0(\bar{\sigma}\alpha_i, \nabla \alpha_j)_\Omega \\ i\omega\mu_0(\bar{\sigma}\nabla \alpha_i, \alpha_j)_\Omega^T & i\omega\mu_0(\bar{\sigma}\nabla \alpha_i, \nabla \alpha_j)_\Omega \end{pmatrix}, \quad (16)$$

where α_i is a linear basis function associated with node i and I_{33} is the 3×3 identity matrix. Considering that \mathbf{K} is symmetric (but non-Hermitian) and not symmetric positive definite (SPD), in Subsection 3.3 we make a selection of appropriate iterative techniques that can handle a system with such characteristics. Condition number of \mathbf{K} strongly depends on the particular problem with many factors affecting it, in particular the presence of air in the model. The fact that the off-diagonal elements of \mathbf{K}_{ij} are several orders of magnitude smaller than the other terms is used to create a more efficient preconditioner.

The right-hand side vector \mathbf{b} represents the source contribution and is of the form $\mathbf{b} = (\mathbf{b}_1, \dots, \mathbf{b}_n)^T$, where

$$\mathbf{b}_i = -i\omega\mu_0 \left(\sum_k A_{pxk}(\Delta\sigma_x \alpha_i, \alpha_k)_\Omega, \sum_k A_{pyk}(\Delta\sigma_y \alpha_i, \alpha_k)_\Omega, \sum_k A_{pzk}(\Delta\sigma_z \alpha_i, \alpha_k)_\Omega, \sum_k \left[A_{pxk} \left(\Delta\sigma_x \frac{\partial \alpha_i}{\partial x}, \alpha_k \right)_\Omega + A_{pyk} \left(\Delta\sigma_y \frac{\partial \alpha_i}{\partial y}, \alpha_k \right)_\Omega + A_{pzk} \left(\Delta\sigma_z \frac{\partial \alpha_i}{\partial z}, \alpha_k \right)_\Omega \right] \right)^T. \quad (17)$$

The sparsity of matrix \mathbf{K} is determined by the mesh node connectivity (the integrals in (16) are zero if node i is not connected to node j through an edge). Each sub-vector \mathbf{b}_i is also zero if node i belongs only to the elements with the conductivity equal to the background one.

3 IMPLEMENTATION DETAILS

3.1 Mesh Generation

The tetrahedral meshes required by our FE scheme were created using ANSYS ICEM CFD mesh generation software. A proper size of the mesh elements is chosen by the skin depth criteria. The meshes are refined in regions where electromagnetic field gradients are expected to be large or where high accuracy is required, such as close to the source or receivers, whereas at distances of a few skin depths the tetrahedra are quite large and keep growing towards the computational boundaries, which are typically located far away to make the boundary effects negligible (Um et al.

2012). The use of unstructured meshes has the advantage of greatly optimizing the number of elements without affecting the solution precision. On the other hand, using unstructured meshes can slow the convergence rate (Subsection 4.5). Our program supports different types of elements which makes it easy to shape very irregular geometries. For tetrahedral meshes ICEM supports both Octree and Delaunay tetrahedral mesh generation techniques (Fig. 1).

In order to perform speedup tests and study solver convergence on large meshes, we use in this work the mesh multiplication (MM) strategy discussed in Houzeaux et al. (2012). The MM strategy consists in subdividing recursively the elements of the original mesh (referred to as zero-level mesh) in parallel. When using tetrahedra, new nodes are added only on edges and faces and the number of elements is multiplied by 8 at each MM level. In the previous reference, starting with a 30 million tetrahedra element mesh a 1.92 billion element mesh was obtained in a few seconds after 2 MM levels.

3.2 Primary potentials

The most commonly used nowadays CSEM sources are horizontal electric dipoles, typically 50–300 meters long, which are often approximated as point dipoles (Streich & Becken 2011). Coulomb-gauged primary potentials for a horizontal electric dipole were derived from the Lorentz-gauged potentials by Liu et al (2010). Slowly-convergent integrals of this type are usually calculated using Hankel transform filters (Kong 2007). For the case of a homogeneous media described by a uniform electrical conductivity $\bar{\sigma}_0$ we have found the expressions for the primary potentials in the closed form:

$$\begin{aligned} A_{0,x} &= \frac{Id\mu_0}{4\pi} \frac{e^{ik_{0x}R}}{R} - \frac{Id}{4i\pi\sigma_{0x}\omega} \frac{e^{ik_{0x}R}}{R^5} \left(x^2 \left(k_{0x}^2 R^2 + 3ik_{0x}R - 3 \right) + R^2 - ik_{0x}R^3 \right), \\ A_{0,y} &= -\frac{Id}{4i\pi\sigma_{0y}\omega} \frac{xye^{ik_{0y}R}}{R^5} \left(k_{0y}^2 R^2 + 3ik_{0y}R - 3 \right), \\ A_{0,z} &= -\frac{Id}{4i\pi\sigma_{0z}\omega} \frac{x(z-z_s)e^{ik_{0z}R}}{R^5} \left(k_{0z}^2 R^2 + 3ik_{0z}R - 3 \right), \\ \Psi_0 &\equiv 0. \end{aligned} \quad (18)$$

Here $R = \sqrt{x^2 + y^2 + (z - z_s)^2}$, $k_{0j}^2 = i\omega\mu_0\sigma_{0j}$, I is the current, d is the dipole length. The details of the transformation are given in Appendix A.

The point source approximation may not represent a real source with necessary precision at short distances. To obtain electromagnetic fields for a finite-length dipole, equations (A1) should be integrated along its length. However, while the actual source geometry is crucial in land CSEM surveys that use kilometer-long source wires, in marine surveys the wire geometry has a small impact on the responses (Streich & Becken 2011). For these reasons, in this paper, dipoles are approximated as point sources and the values of \mathbf{A}_p in each node of the mesh are calculated using the expressions (18).

3.3 Sparse linear system solvers and preconditioning

The linear equation system (15), for typical simulations involving a few millions of elements, is very large and sparse. Since the memory and the computational requirements for solving such a system may seriously challenge even the most efficient direct solvers available today, an interesting alternative is provided by iterative methods. The main advantage of the latter is their low storage requirement, which solves the memory issues of direct methods. Another important benefit is that iterative methods are much easier to implement efficiently on parallel distributed memory computers than direct solvers. Recent discussions on direct and iterative methods can be found in Pardo et al. (2011) and da Silva et al. (2012). Efficiency of the forward-problem solver is critical for its future use inside of a 3-D inversion algorithm since inversion process takes at least two forward solutions per source and per iteration (Commer & Newman 2008; Egbert & Kelbert 2012). Considering that our goal is an as-efficient-as-possible simulation of physical phenomena for three-dimensional models, we use parallel iterative solvers, namely preconditioned complex Krylov subspace methods (Saad 2003).

Despite the symmetry of the system matrix, it is non-Hermitian and not SPD, and hence the conjugate gradient (CG) method cannot be applied. We have implemented three different Krylov subspace methods for complex non-Hermitian linear systems: the complex biconjugate gradient stabilized (BiCGStab), complex quasi-minimal residual (QMR), and complex generalized minimal residual (GMRES) with restarts. The methods differ in storage requirements and the number of calculations required at each iteration. GMRES, a well-known Arnoldi-based method, involves only one matrix-vector multiplication per iteration, but has large storage requirements since an access to all of the previously-generated Arnoldi vectors is required (Saad 2003). BiCGStab (van der Vorst 1992) and QMR (Freund & Nachtigal 1991), two different Lanczos-based approaches, both require two matrix-vector products per iteration (and transpose matrix-vector products in the case of classical QMR), but have minimal storage requirements. A variation of QMR for complex symmetric matrices

exists, which has only one matrix-vector multiplication per iteration and thus significantly minimizes the computational time (e.g., Weiss & Newman 2002). However, symmetric QMR is only applicable if the preconditioner is also symmetric. Other advantages of all three methods, considerations on their convergence and breakdown possibilities are discussed in Saad (2003) and Simoncini & Szyld (2007). All the calculations presented in the following sections have been performed in double complex arithmetic. We also remark that, in order to improve the convergence of the solvers, we have implemented their right-preconditioned variants.

Due to the poor performance of the simple Jacobi (diagonal) preconditioning we have implemented a more efficient approximate inverse-based preconditioner. Our selection criteria were that it is efficient in parallel, uses some of the matrix properties and is cheap to compute, while at the same time significantly accelerates the convergence rate. Approximate inverse preconditioning techniques are based on the minimization of the Frobenius norm of the residual matrix

$$F(\mathbf{M}) = \|\mathbf{I} - \mathbf{KM}\|_F^2 = \sum_1^n \|e_j - \mathbf{K}m_j\|_2^2, \quad (19)$$

where matrix \mathbf{M} , whose value $F(\mathbf{M})$ is small, would be a right-approximate inverse of \mathbf{K} . Since \mathbf{K} is very sparse, (19) reduces to n small least squares problems, which can be solved very quickly. However, the resulting matrix will be not-symmetric and hence the symmetric QMR cannot be applied as a solver. The quality of this kind of preconditioners critically depends on the sparsity pattern chosen for \mathbf{M} . Our approach is a variant of the algorithm of Grote & Huckle (1997), based on a preliminary sparsity pattern, however, with quite large tolerance to keep \mathbf{M} very sparse. To further accelerate the performance with respect to accuracy, in the building of \mathbf{M} we use only the diagonal elements of submatrices (16). The effect of the off-diagonal elements, which are several orders of magnitude smaller, on the convergence rate is negligible, while the gains in memory and computations are sufficient. Moreover, in the case of isotropic problems, three of four diagonal elements are equal and hence two of them do not require computation and storage. The construction of this preconditioner, which will be further referred to as a Truncated Approximate Inverse (TAI), normally takes the time of 12–15 (or even less for isotropy) iterations. Since the TAI matrix is very sparse, the cost of each iteration is only ~30% greater than the one with the diagonal preconditioner.

3.4 Parallelization

Parallel computing is a widely used computational strategy for dealing with tasks that are computationally very demanding. We have implemented parallel versions of our complex linear

solvers and proceeded to integrate them into a fully parallel program framework. Our code works under the Alya System (Houzeaux et al. 2009), which has been designed since its inception for large scale supercomputing and supports unstructured meshes made of different types of elements.

The parallelization strategy of Alya is based on a mesh partitioning technique (also referred to as substructuring) using the Message Passing Interface (MPI) programming paradigm for communication between computational nodes (Gropp et al. 1996). The idea is to partition the original problem domain, which normally consists of a huge number of elements, into smaller subdomains. Thanks to this partitioning, many computations can be done simultaneously, i.e. in parallel, which may reduce the total execution time of the program substantially. The mesh partitioning inside our code is performed using METIS (Karypis & Kumar 1998), a set of serial programs for partitioning graphs coming from finite element meshes that can provide very good volume to surface ratios and well-balanced subdomains for arbitrary meshes, which is paramount for an efficient parallel solution of finite-element simulations.

To illustrate the principle of the parallelization, let us consider a solution of a generic system (15). In the current parallel implementation, a mesh is divided into different submeshes without overlapping elements. Fig. 2 illustrates the decomposition where we have renumbered the unknowns on the interior nodes of subdomains 1 and 2, respectively, and on the interface nodes on Γ_3 , referred to with sub-index 3. Consequently, the global matrix of the system can be rewritten as

$$\begin{pmatrix} K_{11} & 0 & K_{13} \\ 0 & K_{22} & K_{23} \\ K_{31} & K_{32} & K_{33} \end{pmatrix} \quad (20)$$

In our finite element implementation, the assembly of the matrix is carried out in parallel in such a way that subdomains 1 and 2 bring the following contributions to the global matrix, respectively:

$$K^{(1)} = \begin{pmatrix} K_{11} & K_{13} \\ K_{31} & K_{33}^{(1)} \end{pmatrix}, \quad K^{(2)} = \begin{pmatrix} K_{22} & K_{23} \\ K_{32} & K_{33}^{(2)} \end{pmatrix} \quad (21)$$

The blocks $K_{33}^{(1)}$ and $K_{33}^{(2)}$ represent the interactions between the nodes of subdomains 1 and 2, respectively, on the interface Γ_3 , such that: $K_{33} = K_{33}^{(1)} + K_{33}^{(2)}$. In this way, the global matrix is locally assembled in the subdomains. Now, let us examine what happens in the algebraic iterative solvers. One of the basic operations of classical iterative solvers is the matrix-vector product. On the one hand, using the renumbered global matrix a generic matrix-vector product $\mathbf{y} = \mathbf{K} \mathbf{x}$ gives:

$$\begin{pmatrix} y_1 \\ y_2 \\ y_3 \end{pmatrix} = \begin{pmatrix} K_{11} & 0 & K_{13} \\ 0 & K_{22} & K_{23} \\ K_{31} & K_{32} & K_{33} \end{pmatrix} \begin{pmatrix} x_1 \\ x_2 \\ x_3 \end{pmatrix} = \begin{pmatrix} K_{11}x_1 + K_{13}x_3 \\ K_{22}x_2 + K_{23}x_3 \\ K_{31}x_1 + K_{32}x_2 + K_{33}x_3 \end{pmatrix} \quad (22)$$

On the other hand, using the two local contributions $K_{33}^{(1)}$ and $K_{33}^{(2)}$, computed in subdomains 1 and 2 respectively, we observe that two contributions of the matrix-vector product can be computed independently like:

$$\begin{pmatrix} y_1 \\ y_3^{(1)} \end{pmatrix} = \begin{pmatrix} K_{11}x_1 + K_{13}x_3 \\ K_{31}x_1 + K_{33}^{(1)}x_3 \end{pmatrix}, \quad \begin{pmatrix} y_2 \\ y_3^{(2)} \end{pmatrix} = \begin{pmatrix} K_{22}x_2 + K_{23}x_3 \\ K_{32}x_2 + K_{33}^{(2)}x_3 \end{pmatrix} \quad (23)$$

As we have that $K_{33} = K_{33}^{(1)} + K_{33}^{(2)}$, then $y_3 = y_3^{(1)} + y_3^{(2)}$. The matrix-vector product can therefore be computed in parallel in the following way:

1. Using the locally assembled matrices, compute the local matrix-vector product.
2. Sum up the local contributions on the interface unknowns.

The second operation means that a communication is necessary between the subdomains. This communications are carried out using the MPI function `MPI_Sendrecv`. The second step can be summarized as follows:

1. Communication $\Omega_1 \xrightarrow{y_3^{(1)}} \text{MPI_Sendrecv} \xleftarrow{y_3^{(2)}} \Omega_2$	2. Sum up contribution $\Omega_1: y_3^{(1)} \Leftarrow y_3^{(1)} + y_3^{(2)}$ $\Omega_2: y_3^{(2)} \Leftarrow y_3^{(2)} + y_3^{(1)}$
--	--

This procedure can be applied to any number of subdomains, provided that all the subdomains exchange their contribution to the matrix-vector product with all their neighbors (the subdomains that share at least one node with them). One important point at this stage is to schedule the communications to minimize the total time of communication, as the algebraic solver may require the matrix-vector product to be completed before going on. For example, it is usual that the next operation is a scalar product. The scalar product is first computed locally in each subdomain. Then the complete result is assembled using the MPI function `MPI_Allreduce`. The only point to worry about is that the scalar product on interface nodes is not duplicated.

To summarize, the parallelization works in the following way:

1. Assembly: Assemble the local matrix and RHS in each subdomain
2. Algebraic Solver:
 - a. Exchange RHS contributions on the interface nodes using `MPI_Sendrecv` such that each subdomain has the global RHS value on the interface nodes.

- b. Carry out matrix-vector products locally and then exchange contributions on the interface nodes using MPI_Sendrecv.
- c. Carry out scalar products locally and assemble contributions using MPI_Allreduce.

3.5 Moving Least-Squares Interpolation

Our FE code computes the secondary EM potentials (\mathbf{A}_s, Ψ_s) , from which we have to obtain the physically significant fields $(\mathbf{E}_s, \mathbf{H}_s)$. To do this, it is necessary to perform numerical differentiation, for which we follow Badea et al. (2001) and use the Moving Least Squares (MLS) interpolation scheme. The Gaussian function (Alexa et al. 2003) has been chosen to be the weighting function $\theta(d)$

$$\theta(d) = e^{-\frac{d^2}{h^2}} \quad (24)$$

In order to validate MLS interpolation and primary potentials generation, the result of their numerical differentiation has been compared with the fields computed by the analytical formulas (Ward & Hohmann 1988).

For the tests described below, spatial derivatives of the EM potentials were obtained from their FE-computed values at the $n = 50$ nearest nodes to the test point. This parameter, as well as h in the weighting function, controls the smoothness of the result, choosing between a local approximation and smoothing out sharp features for a more global approximation.

4 NUMERICAL RESULTS

In this section, we present four numerical examples which illustrate that our scheme can accurately solve the coupled vector-scalar potential formulation for both current loop and electric dipole sources for very large meshes.

4.1 Comparison with the analytic solution

In order to verify the accuracy of our FE algorithm, we first test it on a borehole model consisting of two half-spaces proposed by Badea et al. (2001). Despite the symmetry of the problem

we choose to solve it on a completely unstructured tetrahedral mesh and compare the results obtained at the model's symmetry axis with the analytical solution to the problem. The source is a horizontal finite-loop transmitter of radius of 0.01 m, placed 1.5 m below an interface separating two conducting materials. The loop carries a current of 10^{10} A oscillating at 2.5 MHz. Primary potentials associated with this kind of source (Eq. (13) of Badea et al. 2001) were evaluated using Hankel transform filters. The conductivities of the lower and upper half-spaces are $\sigma_0 = 0.1$ S/m and $\sigma_1 = 1$ S/m, respectively. The solution domain is a cylinder with radius $R = 9$ m and length $L = 20.35$ m and the skin depth in the lower, less conductive and containing the source, half-space is $z_{s0} = \sqrt{2/\sigma_0\mu_0\omega} \approx 1$ m. The mesh has a strong refinement near the source and along the z -axis in order to resolve better the rapidly varying electric field, the number of nodes is 93 406 (373 624 degrees of freedom in the system). All three solvers with TAI converge to the relative error of 10^{-7} in 500–600 iterations running approximately 15–20 seconds on 4 CPUs.

The vertical magnetic field component (H_z) along the z -axis is compared to the corresponding analytical solution (Ward & Hohmann 1988) in Fig. 3a. The results clearly show a good agreement between the analytical and numerical solutions. In addition, we performed tests for two analogous models with different conductivity contrasts ($\sigma_1/\sigma_0 = 100$ and $\sigma_1/\sigma_0 = 10^5$). In both cases, we obtained numerical results that very precisely match the analytical solutions (the second one is illustrated in Fig. 3b). These results prove that our approach is able to deal with strong conductivity contrasts that might appear in realistic models.

4.2 Comparison with the flat seafloor model

Our next numerical example is a comparison with the results presented by Schwarzbach et al. (2011), who describe a flat seafloor model. Similar to the last example, this case also displays a simple geometry: two half-spaces that represent seawater ($\sigma_0 = 3.3$ S/m) and sediments ($\sigma_1 = 1.0$ S/m) are separated by a planar interface. Unlike the previous case, the source now is an x-directed horizontal electric dipole radiating with frequency 1 Hz, placed 100 m above the seafloor at $(0, 0, -100)$. The source dipole moment (product of the current and the dipole length) is 1 Am, which, for a finite dipole of a length that is small compared to the source-receiver separation, is proportional to the amplitude of the field at the receiver. The computational domain $\Omega = \{-2\text{ km} \leq x, y \leq 2\text{ km}; -1.5\text{ km} \leq z \leq 2.5\text{ km}\}$ has been chosen according to Schwarzbach

et al. (2011) to compare our results with their ones. The background conductivity model was considered homogeneous with the conductivity of the seawater ($\sigma_0 = 3.3 \text{ S/m}$).

Two meshes have been considered for this model. The small one has 98 031 nodes (and hence the system to be solved has 392 124 degrees of freedom) and 565 811 elements. The average size of the elements ranges from 10 m near the source to 250 m at the boundaries of the domain (the skin depth in water is 277 m). The finer mesh has 533 639 nodes (2 134 556 degrees of freedom) and 3 121 712 elements of average size ranging from 6 to 100 meters. Due to the low memory requirements of iterative linear solvers, the total amount of allocated memory was 3.9 GB for the large mesh simulation and less than 0.7 GB for the small one. Convergence of the solvers is discussed in Subsection 4.5.

Absolute values and phases of the non-vanishing secondary electric and magnetic field components in the X - Z plane at $y=0$ are shown in Fig. 4. These results are remarkably similar to those of Schwarzbach et al. (2011, Fig. 5), even when computed with the small, i.e. coarse, mesh (results for the finer mesh are similar, only with a slightly higher accuracy). The other three components H_x , E_y and H_z along an inline profile through the center of the model should vanish for symmetry reasons. Our results for these components contain only numerical noise, which is 2-3 (for the small mesh) or 3-4 (for the finer mesh) orders of magnitude lower than those presented in Fig. 4.

4.3 Canonical disc model

In CSEM the operating frequencies of a transmitter may range between 0.1 and 10 Hz, the choice being determined by the model's dimensions. In most studies, typical frequencies vary from 0.25 to 1 Hz. For source-receiver offsets up to 10-12 km, the penetration depth of the method can extend to several kilometers below the seafloor (MacGregor & Sinha 2000; Eidesmo et al. 2002). In this subsection we perform simulations of a well-known canonical disc model, as proposed by Weiss & Constable (2006). This model was also recently studied by Schwarzbach et al. (2011), who compared the results of their FE simulation with those of Weiss's finite-volume code FDM3D and added an air half-space in the model to study the airwave effect.

The canonical disc model consists of two half-spaces that represent 1.5 km deep seawater ($\sigma_0 = 3.3 \text{ S/m}$) and sediments ($\sigma_1 = 1.0 \text{ S/m}$), and a disc of 2 km radius and 100 m height located 1 km beneath the interface that is a simplified model of a hydrocarbon reservoir ($\sigma_2 = 0.01 \text{ S/m}$). The transmitter is a horizontal electric dipole oriented in x-direction, operating at

a frequency of 1 Hz and placed at coordinates $(-3000, 0, -100)$. We measure the electromagnetic field values along an inline profile through the center of the model. The model with the air half-space has the same characteristics, except the 1 km thick water layer and a much larger computational domain. A plan view of these models is given in Fig. 8 of Schwarzbach et al. (2011). As noted by the authors of that paper, the results are largely influenced by the choice of a background conductivity model for the primary field, so here we also choose a homogeneous one.

The model responses obtained through the use of our finite-element method are presented in Fig. 5. As in the original paper, four simulations were performed: with the hydrocarbon reservoir and without it ($\sigma_2 = \sigma_1$) and including the air half-space or not. The electromagnetic field decays rapidly in a conductive medium and, therefore, the secondary field usually is much smaller than the primary one. In many cases, this leads to the situation where the difference between the results of the simulations with and without hydrocarbon reservoir is quite small and the target field is partially hidden in the background field. Here, as in Fig. 9 of Schwarzbach et al. (2011), the fields are indistinguishable for a transmitter/receiver distance smaller than 2.5 km. Further comparison with their results shows that both numerical solutions are in good agreement. The fields decay slower if the resistive disc is included in the model. The presence of the air half-space has a little effect on the vertical electric component, however its influence is significant for the horizontal field components at the offsets larger than 4.5 km. The discussion on different sensitivity of horizontal and vertical electric field components to the air can be found, for example, in Andreis & MacGregor (2008).

The mesh used for the simulations with the air half-space has \sim 0.5 million of nodes and \sim 3 millions of elements. We also performed the simulations with an automatic mesh refinement of levels 1 and 2 (at each subsequent level, each tetrahedron is divided into 8). The mesh of second-level refinement has \sim 192 millions of elements and \sim 128 millions of degrees of freedom that can be considered as a computationally highly demanding problem nowadays. The solution times and memory consumption for these simulations are given in Table 1. In all tests, the number of solver iterations was limited to 800. Memory consumption is low and grows linearly with the mesh size thanks to the use of iterative solvers. Scalability of the code for this model is studied in Subsection 4.6.

4.4 Complex synthetic model

To illustrate the possibilities to handle arbitrary seafloor bathymetry and geological complexity with unstructured tetrahedral meshes, we create and test a realistic synthetic model (Fig. 6). The dimensions of the model are 18x15x8 km, water depth has variations from 1050 to

1200 m. A 1 Hz dipole is placed at $x = -2$ km, 60 m above the seafloor. The conductivities of all layers are given in Table 2. Since bathymetry effects on the measured fields, if not accounted for, can produce large anomalies (Hoversten et al. 2006), we need an accurate seafloor representation. Several meshes were created for this problem, the one that offers stable results without numerical noise (compared to better meshes) has 2.8 million of elements ranging from 8 to 400 meters. The solver converged to 10^{-8} in about 1200–1400 iterations (~ 1.5 minutes on 16 CPUs) for different model parameters.

To illustrate the effect of anisotropic conductivity in the data, we also performed simulations for the isotropic model (with the conductivities equal to σ_h from Table 2). The inline responses of both anisotropic and isotropic models are presented in Fig. 7 in the form of the absolute values of the secondary fields (top row) and normalized by the corresponding results of the simulation without the reservoir (bottom row). One can see that the normalized curves for both electric and magnetic fields vary significantly with the change in vertical conductivity. The growth of normalized inline electric field values for similar anisotropy coefficient was also observed in Kong et al. (2008).

4.5 Convergence of the solvers

In general, the convergence of Krylov subspace methods is heavily dependent upon the condition number of the matrix. Matrices with small condition numbers tend to converge rapidly, whereas those with large ones converge much slower. Various preconditioning techniques are used to accelerate a slow convergence of Krylov methods. Different linear solvers can also compete in terms of convergence rate and computational cost of each iteration. In this subsection we study the performance of right-preconditioned BiCGStab, QMR and GMRES methods with diagonal and TAI preconditioners for the problems described above. The convergence plot in Fig. 8 shows the norms of BiCGStab and QMR residuals versus the iteration number for the small mesh described in Subsection 4.2. One can observe a good convergence rate: the relative errors reach 10^{-12} after ~ 900 iterations of BiCGStab with the simple diagonal preconditioner. The performance of TAI is approximately 3 times better in terms of iterations or 2.3 times in terms of computational time.

Unstructured meshes are usually refined in the vicinity of the source and receivers to get more accurate solutions. On the other hand, large aspect ratios of the mesh elements can cause slow convergence rate. Larger linear systems (millions of degrees of freedom) converge slower as well. BiCGStab and QMR performance on the canonical disc model without automatic mesh refinement (~ 2 millions of degrees of freedom) is illustrated in Fig. 9. Due to the size of the domain this mesh has quite large aspect ratios of the elements, which results in bad convergence rate for the diagonal

preconditioner, though with TAI relative residual norms reach about 10^{-8} in less than 1000 iterations. Fig. 10 shows the comparison of all three solvers with TAI for the flat seafloor and canonical disc models. The residual norm of GMRES without restarts decreases monotonically and the convergence is smooth, however BiCGStab with its oscillations performs better or equal. Due to the large memory and computational requirements of the former, there seems to be no reason to use it in real simulations. QMR, quite popular solver in the community, can reach BiCGStab after several hundreds or thousands of iterations, though at the beginning its convergence rate is much worse. However, if the matrix and preconditioner are both symmetric, iterations of the symmetric QMR will be computationally less expensive. In other cases, we suggest using BiCGStab in combination with a proper preconditioner for this class of problems.

4.6 Scalability tests

Our simulations have been carried out on the MareNostrum III supercomputer (<http://www.bsc.es>), which has 48448 Intel E5-2670 cores running at 2.6 GHz, 94 TB of main memory (2 GB per core, 32 GB per node), Infiniband FDR10 interconnection network and is running under Linux. The scalability of the code has been verified by running the problem discussed in Subsection 4.3 with the same number of solver iterations for different numbers of CPUs working in parallel. We have measured the total time spent on the construction of the system matrix and on solving the system. The first part takes approximately 1% of the total time, so that most of the CPU usage involves the solver of the linear system. Due to the memory requirements, we start the simulations for the large meshes with first- and second-level refinements on 8 and 80 MareNostrum cores, respectively.

The simulations for the first-level mesh have been carried out consecutively on 8, 16, 32, 64, 128, 256, 512 and 1024 CPUs as shown in Fig. 11a. The simulation on 8 slaves took 15 minutes (one should keep in mind that the size of the system is \sim 16 millions of degrees of freedom), while on 128 slaves the time spent was 1.5 minutes. After a slight decrease at 16 CPUs the achieved speed-up is close to linear until 128 processors. From this number, the speed-up stops its near-linear growth and slowly begins to saturate. At this point, increasing the number of nodes is not that efficient since each of the sub-domains has less than 100 000 elements and the execution becomes dominated by message passing, though the speed-up remains growing constantly.

The results of the scalability tests for the second-level mesh are illustrated in Fig. 11b. For 160 and 320 CPUs the achieved speed-up is almost linear. From 640 processors the growth becomes a bit slower but still constant.

5 CONCLUSIONS

We have presented a finite-element solution to electromagnetic problems in the frequency domain involving active sources, either current loops or dipoles. The finite-element approach, when used with the support of completely unstructured meshes makes irrelevant the geological and bathymetric complexity of the models simulated and hence has a very broad range of applicability for real case scenarios. We have demonstrated with examples that the method is well suited to solve large CSEM forward problems accurately and efficiently. The method supports electrical anisotropy that is known to have a possible heavy impact on the inversion process.

In addition, explicit and closed expressions of the primary potentials have been developed for the case of dipole point sources, which are the most important source class for CSEM problems. Similarly, we have presented an effective preconditioner well suited for this kind of complex Helmholtz-type equation systems and outlined and discussed the solvers employed as well as shown their convergence and scalability. For the problems under consideration the BiCGStab method outperformed the other techniques in terms of convergence and computational costs. Finally, due to the usage of parallel Krylov subspace solvers and preconditioners, and a good program design, the scheme can display extremely good performance in terms of scalability for large parallel applications.

In order to exploit CSEM data in areas of complex geology for practical applications, it is important to create reliable and efficient tools both for 3-D forward modeling and inversion. As a consequence, our next development steps will concentrate on solving 3-D inverse problems based upon the forward modeling scheme presented here. Last but not least, we acknowledge the fact that inverting a single data type in hydrocarbon exploration could result in ambiguities in the interpretation. Therefore we aim at integrating in the future different geophysical datasets, e.g. seismic and EM, in order to reduce the uncertainty in the characterization of subsurface properties.

ACKNOWLEDGMENTS

Funding for this work was provided by the Repsol-BSC Research Center. The authors acknowledge Repsol for permission to submit this paper. All numerical tests were performed on MareNostrum Supercomputer of the Barcelona Supercomputing Center. VP wishes to express his gratitude for hospitality during his visit to Texas A&M University. The authors would like to thank

Dr. Christoph Schwarzbach for providing additional information on their results and the Editor, Dr. Gary Egbert, and two anonymous reviewers for their suggestions that helped to improve the presentation of this paper.

REFERENCES

1. Abubakar, A., Habashy, T.M., Druskin, V.L., Knizhnerman, L. & Alumbaugh, D., 2008. 2.5D forward and inverse modeling for interpreting low-frequency electromagnetic measurements, *Geophysics*, **73**(4), F165–F177.
2. Alexa, M., Behr, J., Cohen-Or, D., Fleishman, S., Levin, D. & Silva, C.T., 2003. Computing and rendering point set surfaces, *IEEE Trans. Vis. Comput. Graphics*, **9**(1), 3–15.
3. Andreis, D. & MacGregor, L., 2008. Controlled-source electromagnetic sounding in shallow water: principles and applications, *Geophysics*, **73**(1), F21–F32.
4. Avdeev, D.B., 2005. Three-dimensional electromagnetic modelling and inversion from theory to application, *Surv. Geophys.*, **26**, 767–799.
5. Avdeev, D.B., Kuvshinov, A.V., Pankratov, O.V., & Newman, G.A., 1997. High performance three dimensional electromagnetic modeling using modified Neumann series: Wide band numerical solution and examples, *J. Geomag. Geoelectr.*, **49**, 1519–1539.
6. Badea, E.A., Everett, M.E., Newman, G.A. & Biro, O., 2001. Finite-element analysis of controlled-source electromagnetic induction using Coulomb-gauged potentials, *Geophysics*, **66**(3), 786–799.
7. Biro, O., & Preis, K., 1989. On the use of the magnetic vector potential in the finite element analysis of three-dimensional eddy currents, *IEEE Trans. Magn.*, **25**, 3145–3159.
8. Borner, R.U., 2010. Numerical modelling in geo-electromagnetics: advances and challenges, *Surv. Geophys.*, **31**(2), 225–245.
9. Burnett, D.S., 1987. *Finite element analysis: from concepts to applications*, Addison Wesley.
10. Chave, A.D. & Cox, C.S., 1982. Controlled electromagnetic sources for measuring electrical conductivity beneath the oceans. 1. Forward problem and model study, *J. Geophys. Res.*, **87**, 5327–5338.
11. Commer, M. & Newman, G.A., 2008. New advances in three-dimensional controlled-source electromagnetic inversion, *Geophys. J. Int.*, **172**, 513–535.
12. Constable, S., 2010. Ten years of marine CSEM for hydrocarbon exploration, *Geophysics*, **75**(5), A67–A81.

13. Constable, S. & Srnka, L.J., 2007. An introduction to marine controlled source electromagnetic methods for hydrocarbon exploration, *Geophysics*, **72**(2), WA3–WA12.
14. da Silva, N.V., Morgan, J.V., MacGregor, L. & Warner, M., 2012. A finite element multifrontal method for 3D CSEM modeling in the frequency domain, *Geophysics*, **77**(2), E101–E115.
15. Davydycheva, S., Druskin, V. & Habashy, T., 2003. An efficient finite-difference scheme for electromagnetic logging in 3D anisotropic inhomogeneous media, *Geophysics*, **68**, 1525–1536.
16. Edwards, N., 2005. Marine controlled source electromagnetics: principles, methodologies, future commercial applications, *Surv. Geophys.*, **26**(6), 675–700.
17. Egbert, G.D. & Kelbert, A., 2012. Computational recipes for electromagnetic inverse problems, *Geophys. J. Int.*, **189**, 251–267.
18. Eidesmo, T., Ellingsrud, S., MacGregor, L.M., Constable, S., Sinha, M.C., Johansen, S., Kong, F.N. & Westerdahl, H., 2002. Sea Bed Logging (SBL), a new method for remote and direct identification of hydrocarbon filled layers in deepwater areas, *First Break*, **20**, 144–152.
19. Everett, M.E., 2012. Theoretical developments in electromagnetic induction geophysics with selected applications in the near surface, *Surv. Geophys.*, **33**, 29–63.
20. Farquharson, C.G. & Miensopust, M.P., 2011. Three-dimensional finite-element modelling of magnetotelluric data with a divergence correction, *J. Appl. Geophys.*, **75**, 699–710.
21. Franke, A., Borner, R.U. & Spitzer, K., 2007. Adaptive unstructured grid finite element simulation of two-dimensional magnetotelluric fields for arbitrary surface and seafloor topography, *Geophys. J. Int.*, **171**(1), 71–86.
22. Freund, R.W. & Nachtigal, N.M., 1991. QMR: a quasi-minimal residual method for non-Hermitian linear systems, *Numer. Math.*, **60**, 315–339.
23. Gropp, W., Lusk, E., Doss, N. & Skjellum, A., 1996. A high-performance, portable implementation of the MPI message passing interface standard, *Parallel Comput.*, **22**, 789–828.
24. Grote, M.J. & Huckle, T., 1997. Parallel preconditioning with sparse approximate inverses, *SIAM J. Sci. Comput.*, **18**, 838–853.
25. Haber, E., Ascher, U.M., Aruliah, D.A. & Oldenburg, D.W., 2000. Fast simulation of 3D electromagnetic problems using potentials, *J. Comput. Phys.*, **163**(1), 150–171.
26. Houzeaux, G., Vazquez, M., Aubry, R. & Cela, J.M., 2009. A massively parallel fractional step solver for incompressible flows, *J. Comput. Phys.*, **228**, 6316–6332.
27. Houzeaux, G., de la Cruz, R., Owen, H. & Vazquez, M., 2012. Parallel uniform mesh multiplication applied to a Navier-Stokes solver, In Press, *Computers & Fluids*.

28. Hoversten, G.M., Newman, G.A., Geier, N. & Flanagan, G., 2006. 3D modeling of a deepwater EM exploration survey, *Geophysics*, **71**(5), G239–G248.
29. Karypis, G. & Kumar, V., 1998. A fast and high quality multilevel scheme for partitioning irregular graphs, *SIAM J. Sci. Comput.*, **20**(1), 359–392.
30. Key, K., 2012. Marine electromagnetic studies of seafloor resources and tectonics, *Surv. Geophys.*, **33**, 135–167.
31. Key, K. & Ovall, J., 2011. A parallel goal-oriented adaptive finite element method for 2.5-D electromagnetic modeling, *Geophys. J. Int.*, **186**(1), 137–154.
32. Key, K. & Weiss, C., 2006. Adaptive finite element modeling using unstructured grids: the 2D magnetotelluric example, *Geophysics*, **71**(6), G291–G299.
33. Kong, F.N., 2007. Hankel transform filters for dipole antenna radiation in a conductive medium, *Geophys. Prospect.*, **55**, 83–89.
34. Kong, F.N., Johnstad, S.E., Rosten, T. & Westerdahl, H., 2008. A 2.5D finite-element-modeling difference method for marine CSEM modeling in stratified anisotropic media, *Geophysics*, **73**(1), F9–F19.
35. Li, Y. & Key, K., 2007. 2D marine controlled-source electromagnetic modeling, Part 1: an adaptive finite element algorithm, *Geophysics*, **72**(2), WA51–WA62.
36. Li, Y. & Dai, S., 2011. Finite element modelling of marine controlled-source electromagnetic responses in two-dimensional dipping anisotropic conductivity structures, *Geophys. J. Int.*, **185**, 622–636.
37. Liu, C.S., Everett, M.E., Lin, J. & Zhao, F.D., 2010. Modeling seafloor exploration using electric source frequency domain CSEM and the analysis of water depth effect, *Chinese J. Geophys.*, **53**, 669–683.
38. Løseth, L.O. & Ursin, B., 2007. Electromagnetic fields in planarly layered anisotropic media. *Geophys. J. Int.*, **170**, 44–80.
39. MacGregor, L. & Sinha, M., 2000. Use of marine controlled-source electromagnetic sounding for sub-basalt exploration, *Geophys. Prospect.*, **48**, 1091–1106.
40. MacGregor, L., Sinha, M. & Constable, S., 2001. Electrical resistivity structure of the Value Fa Ridge, Lau Basin, from marine controlled-source electromagnetic sounding, *Geophys. J. Int.*, **146**, 217–236.
41. Mitsuhashita, Y. & Uchida, T., 2004. 3D magnetotelluric modeling using the T-Omega finite-element method, *Geophysics*, **69**(1), 108–119.
42. Monk, P., 2003. *Finite element methods for Maxwell's equations*, Oxford University Press.
43. Mukherjee, S. & Everett, M.E., 2011. 3D controlled-source electromagnetic edge-based finite element modeling of conductive and permeable heterogeneities, *Geophysics*, **76**(4), F215–

- F226.
44. Nédélec, J.-C., 1986. A new family of mixed elements in \mathbb{R}^3 , *Numer. Math.*, **50**, 57–81.
 45. Newman, G.A. & Alumbaugh, D.L., 1995. Frequency-domain modelling of airborne electromagnetic responses using staggered finite differences, *Geophys. Prospect.*, **43**, 1021–1042.
 46. Newman, G.A., Commer, M., & Carrazzone, J.J., 2010. Imaging CSEM data in the presence of electrical anisotropy, *Geophysics*, **75**(2), F51–F61.
 47. Pardo, D., Nam, M., Torres-Verdin, C., Hoversten, M. & Garay, I., 2011. Simulation of marine controlled source electromagnetic measurements using a parallel fourier hp-finite element method , *Comput. Geosci.*, **15**, 53–67.
 48. Saad, Y., 2003. *Iterative methods for sparse linear systems*, 2nd ed.: Society for Industrial and Applied Mathematics Philadelphia.
 49. Sasaki, Y. & Meju, M.A., 2009, Useful characteristics of shallow and deep marine CSEM responses inferred from 3D finite-difference modeling, *Geophysics*, **74**(5), F67–F76.
 50. Schwalenberg, K. & Edwards, R.N., 2004. The effect of seafloor topography on magnetotelluric fields: an analytic formulation confirmed with numerical results, *Geophys. J. Int.*, **159**, 607–621.
 51. Schwarzbach, C., Borner, R.-U. & Spitzer, K., 2011. Three-dimensional adaptive higher order finite element simulation for geo-electromagnetics – a marine CSEM example, *Geophys. J. Int.*, **187**, 63–74.
 52. Simoncini, V. & Szyld, D.B., 2007. Recent computational developments in Krylov subspace methods for linear systems, *Numer. Linear Algebra Appl.*, **14**(1), 1–59.
 53. Streich, R. & Becken, M., 2011. Electromagnetic fields generated by finite-length wire sources: comparison with point dipole solutions, *Geophys. Prospect.*, **59**, 361–374.
 54. Streich, R., Becken, M. & Ritter, O., 2011. 2.5D controlled-source EM modeling with general 3D source geometries, *Geophysics*, **76**(6), F387–F393.
 55. Um, E., Harris, J. & Alumbaugh, D., 2012. An iterative finite element time-domain method for simulating three-dimensional electromagnetic diffusion in earth, *Geophys. J. Int.*, **190**, 871–886.
 56. Unsworth, M.J., Travis, B.J. & Chave, A.D., 1993. Electromagnetic induction by a finite electric dipole over a 2-dimensional earth, *Geophysics*, **58**, 198–214.
 57. van der Vorst, H.A., 1992. BI-CGSTAB: a fast and smoothly converging variant of bi-CG for the solution of nonsymmetric linear systems, *SIAM J. Sci. Stat. Comput.* **13**, 631–644.
 58. Wannamaker, P., Hohmann, G. & San Filipo, W., 1984. Electromagnetic modeling of 3-dimensional bodies in layered earths using integral-equations, *Geophysics*, **49**, 60–74.

59. Ward, S.H. & Hohmann, G.W., 1988. Electromagnetic theory for geophysical applications, in *Electromagnetic Methods in Applied Geophysics*, pp. 131–311, ed. N.M. Nabighian, SEG.
60. Weiss, C.J. & Constable, S., 2006. Mapping thin resistors and hydrocarbons with marine EM methods, Part II – Modeling and analysis in 3D, *Geophysics*, **71**(6), G321–G332.
61. Weiss, C.J. & Newman, G.A., 2002. Electromagnetic induction in a fully 3-D anisotropic earth, *Geophysics*, **67**(4), 1104–1114.
62. Weitemeyer, K., Gao, G., Constable, S. & Alumbaugh, D., 2010. The practical application of 2D inversion to marine controlled-source electromagnetic data, *Geophysics*, **75**(6), F199–F211.
63. Zhdanov, M.S. & Fang, S., 1997. Quasi-linear series in three-dimensional electromagnetic modeling, *Radio Sci.*, **32**, 2167–2188.

Table 1. Performance results of the canonical disc model simulations, 800 iterations of BiCGStab+TAI

Level of mesh refinement	Degrees of freedom (mln)	Memory consumption (GB)	Number of slaves	Execution time (s)
0	2.04	3.6	1	852.5
			16	63.5
1	16.0	29.1	8	910.2
			1024	21.7
2	128.0	232.8	80	973.2
			1280	91.4

Table 2. Model conductivities

Layer	σ_h (S/m)	σ_v (S/m)
Water	3.3	
1	1.0	0.67
2	1.2	0.8
3	0.9	0.5
4	0.6	0.25
5	1.0	0.7
Target	0.015	0.01

Figure 1. Slice of the marine CSEM meshes in the X - Z plane generated by Octree (a) and Delaunay (b) mesh generation techniques.

Figure 2. Mesh decomposition example.

Figure 3. A comparison of our FE/MLSI solution against the analytical one for the conductivity contrast of 10 (a) and 10^5 (b). The solid lines represent the real (purple line) and imaginary (black line) parts of the analytic solution. Our solution is marked with blue (real part) and red (imaginary part) circles.

Figure 4. Our solution for a flat seafloor model. Absolute values (top row) and phases (bottom row) of non-vanishing secondary field components in the X - Z plane at $y = 0$.

Figure 5. Non-vanishing secondary field components for the canonical disc model.

Figure 6. Complex synthetic model: seafloor bathymetry (a) and X - Z slice of the central part (b).

Figure 7. Secondary fields for the complex synthetic model: absolute (top row) and normalized (bottom row) values.

Figure 8. Convergence rate of BiCGStab and QMR solvers for the small mesh for the flat seafloor model (0.39 millions of degrees of freedom).

Figure 9. Convergence rate of BiCGStab and QMR solvers for the zero-level mesh for the canonical disc model (2.04 millions of degrees of freedom).

Figure 10. Comparison of BiCGStab, QMR and GMRES solvers with TAI preconditioner for the flat seafloor (left) and canonical disc (right) models.

Figure 11. Scalability study for the first-level (16 millions of degrees of freedom) and the second-level (128 millions of degrees of freedom) meshes.

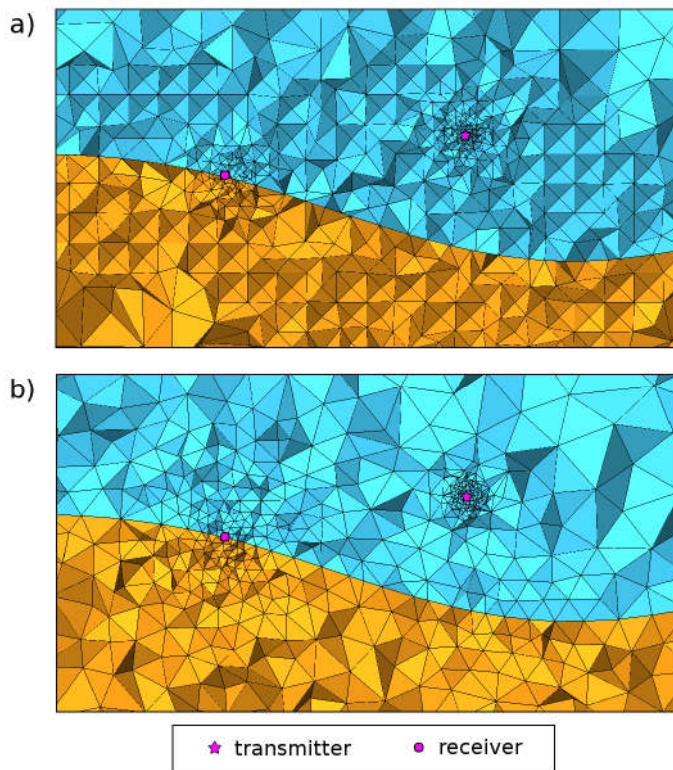


Figure 1.

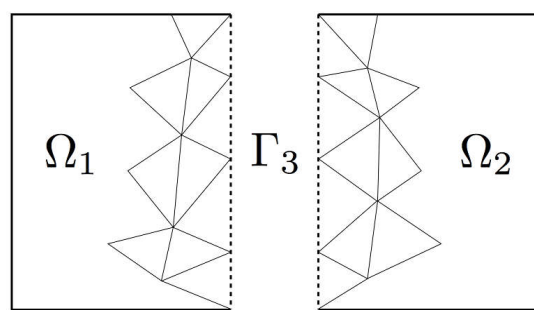


Figure 2.

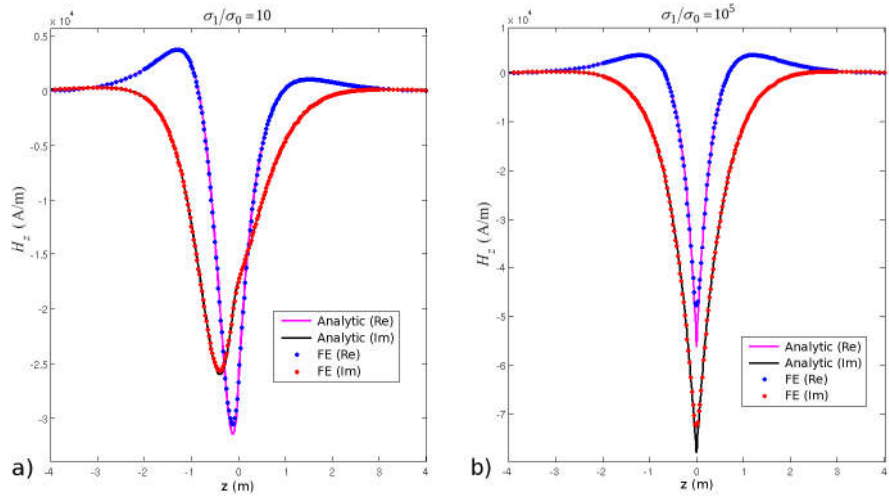


Figure 3.

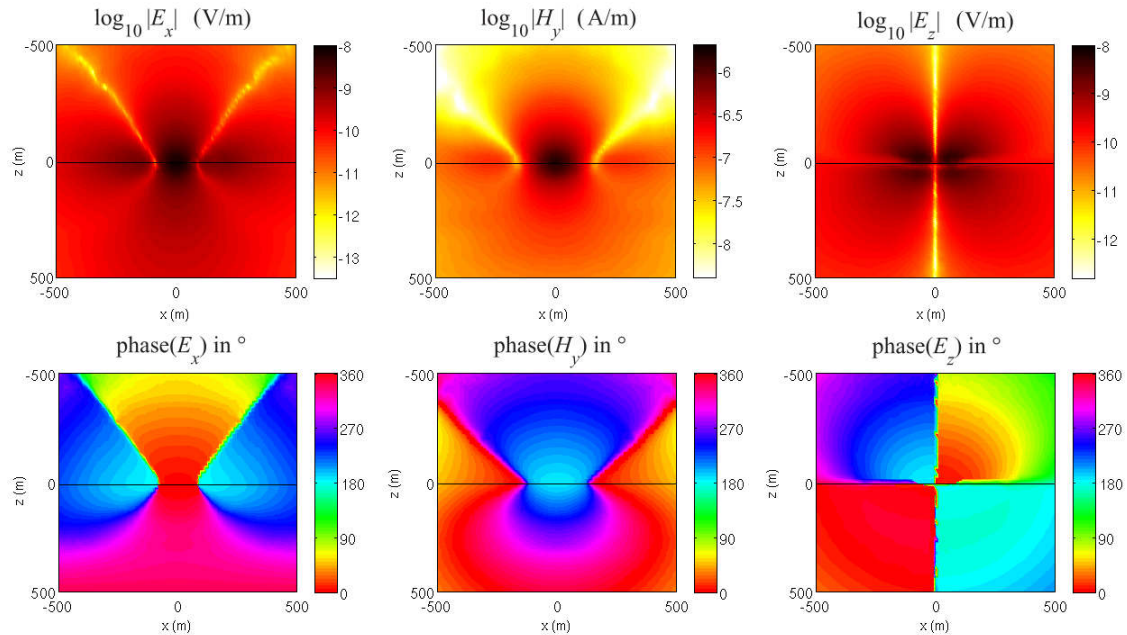


Figure 4.

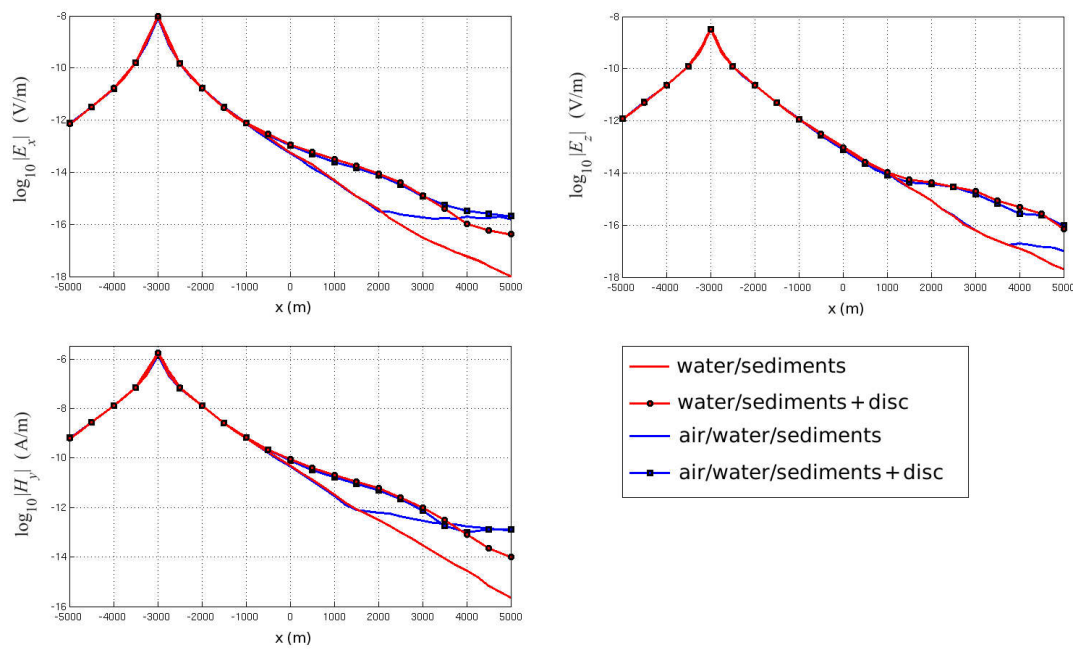


Figure 5.

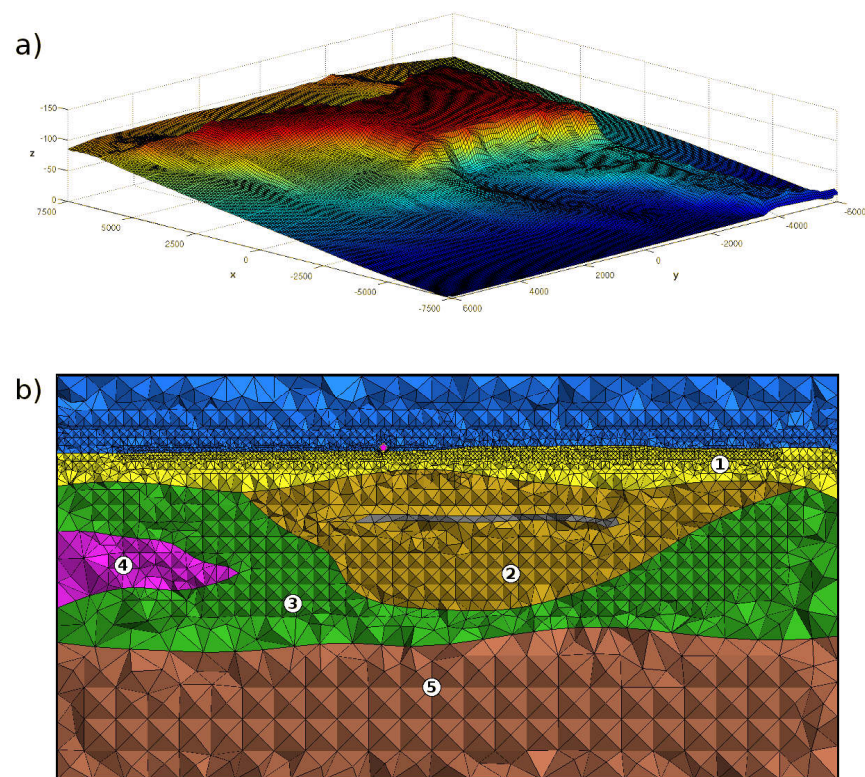


Figure 6.

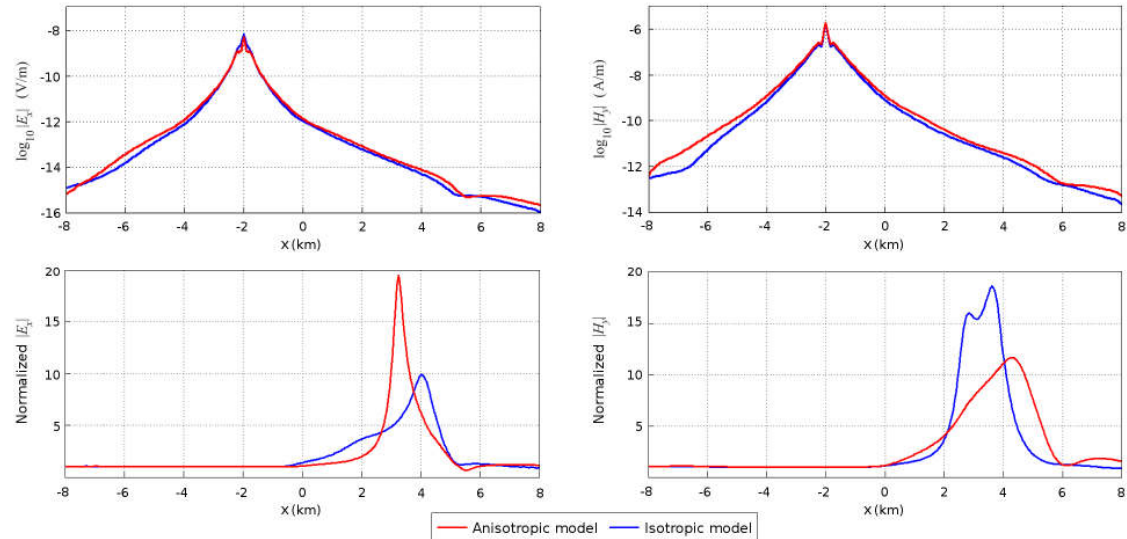


Figure 7.

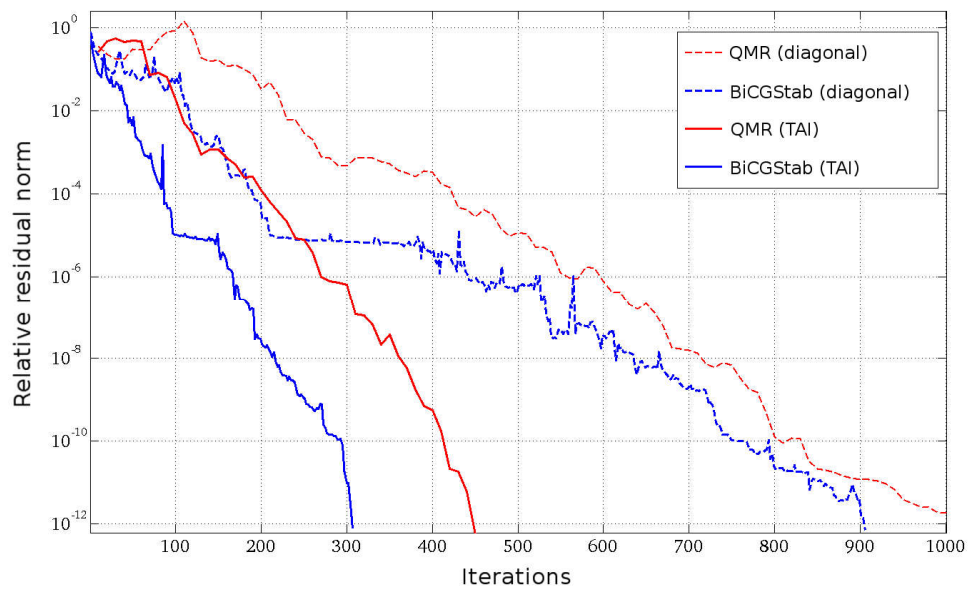


Figure 8.

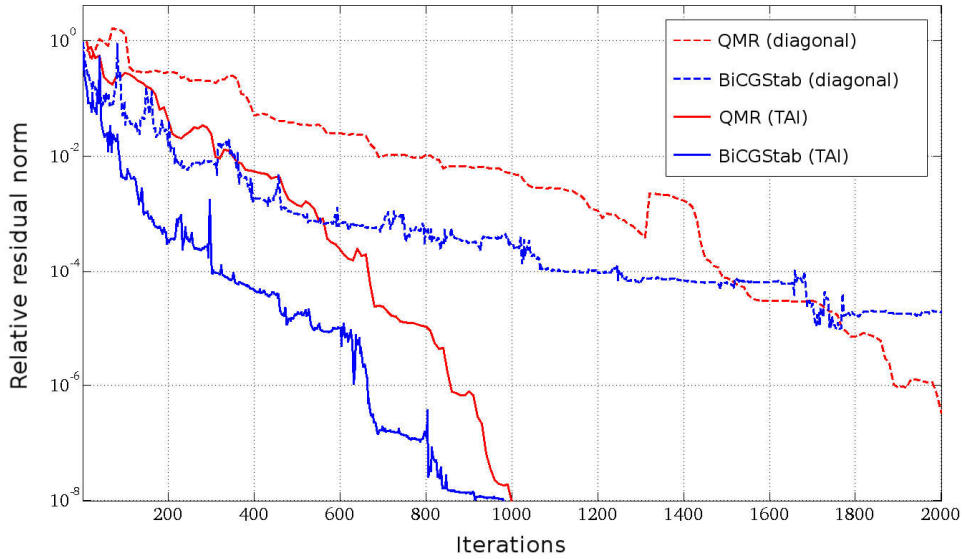


Figure 9.

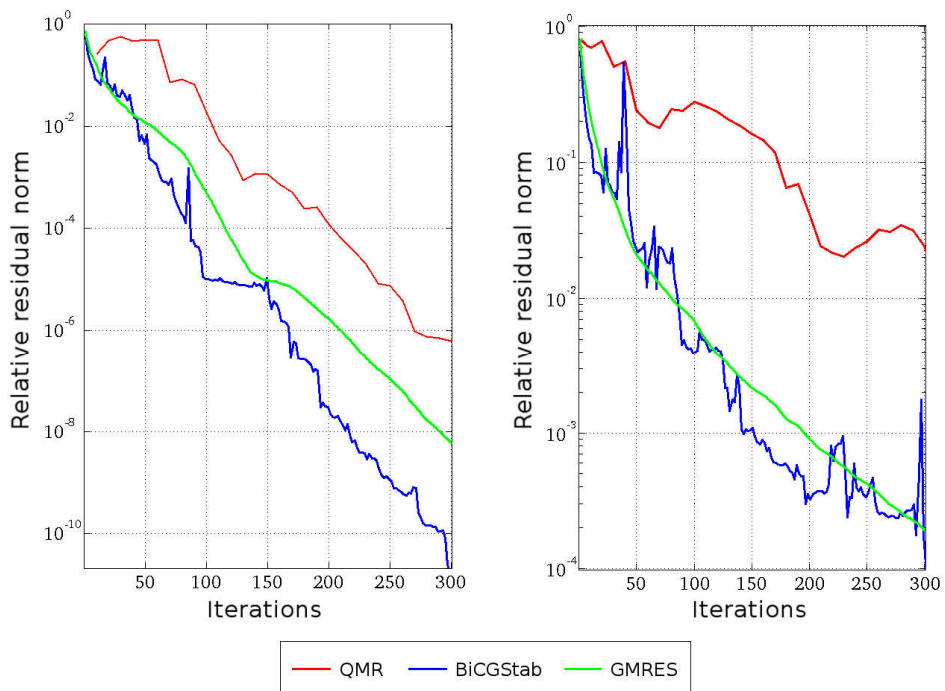


Figure 10.

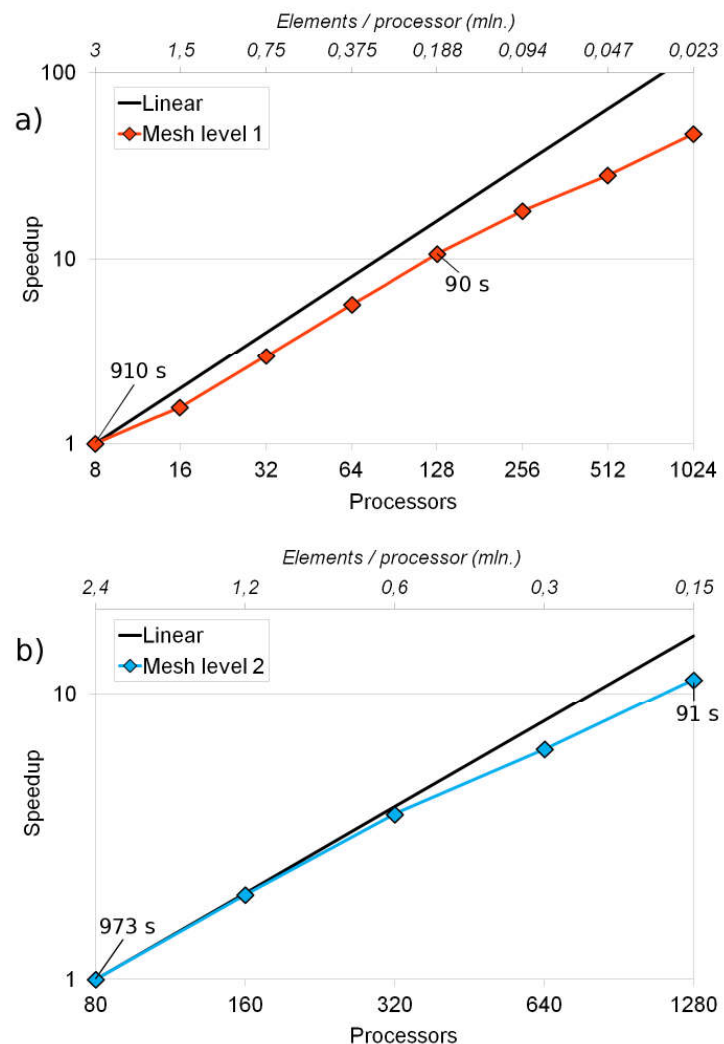


Figure 11.

APPENDIX A: Analytical expressions for primary potentials

Coulomb-gauged primary potentials for a horizontal electric dipole in a homogeneous media are (Liu et al, 2010):

$$\begin{aligned}
 A_{0,x} &= \frac{Id\mu_0}{4\pi} \int_0^\infty \frac{\lambda}{\alpha_0} \cdot e^{-\alpha_0|z-z_s|} \cdot J_0(\lambda\rho) d\lambda + \frac{Id}{4i\pi\sigma_0\omega} \int_0^\infty \frac{\lambda}{\alpha_0} \cdot e^{-\alpha_0|z-z_s|} \cdot \frac{\partial^2}{\partial x^2} J_0(\lambda\rho) d\lambda, \\
 A_{0,y} &= \frac{Id}{4i\pi\sigma_0\omega} \int_0^\infty \frac{\lambda}{\alpha_0} \cdot e^{-\alpha_0|z-z_s|} \cdot \frac{\partial^2}{\partial x \partial y} J_0(\lambda\rho) d\lambda, \\
 A_{0,z} &= \frac{Id}{4i\pi\sigma_0\omega} \int_0^\infty -\text{sign}(z-z_s)\lambda \cdot e^{-\alpha_0|z-z_s|} \cdot \frac{\partial}{\partial x} J_0(\lambda\rho) d\lambda, \\
 \Psi_0 &\equiv 0,
 \end{aligned} \tag{A1}$$

where $a_{0j} = \sqrt{\lambda^2 - k_{0j}^2}$, $\rho = \sqrt{x^2 + y^2}$. They are transformed into (18) using the Sommerfeld identity and derivative relationships (e.g., Ward & Hohmann 1988; Chave & Cox 1982):

$$\begin{aligned}
 \int_0^\infty \frac{\lambda}{\alpha_0} \cdot e^{-\alpha_0|z-z_s|} \cdot J_0(\lambda\rho) d\lambda &= \frac{e^{ik_0 R}}{R}, \\
 \int_0^\infty \frac{\lambda}{\alpha_0} \cdot e^{-\alpha_0|z-z_s|} \cdot \frac{\partial^2}{\partial x^2} J_0(\lambda\rho) d\lambda &= \frac{\partial^2}{\partial x^2} \left(\frac{e^{ik_0 R}}{R} \right), \\
 \int_0^\infty \frac{\lambda}{\alpha_0} \cdot e^{-\alpha_0|z-z_s|} \cdot \frac{\partial^2}{\partial x \partial y} J_0(\lambda\rho) d\lambda &= \frac{\partial^2}{\partial x \partial y} \left(\frac{e^{ik_0 R}}{R} \right), \\
 \int_0^\infty \lambda \cdot e^{-\alpha_0|z-z_s|} \cdot \frac{\partial}{\partial x} J_0(\lambda\rho) d\lambda &= \frac{\partial}{\partial x} \left(\frac{|z-z_s| e^{ik_0 R}}{R^3} (1 - ik_0 R) \right).
 \end{aligned} \tag{A2}$$

In more general cases, the calculation of primary potentials will require the computation of Hankel transforms, which is computationally expensive. The more efficient way to do it is to use Hankel transform filters. In this case, one should keep in mind that these filters have some limitations on the distance, though high-performance ones can evaluate the fields very well within typical source-receiver offsets of CSEM (Kong 2007). Formulas (18) are analytic expressions, they were tested for different values of ρ ranging up to 20 skin depths and, of course, proved to be precise.